Nano Energy 59 (2019) 472–480

Contents lists available at ScienceDirect

Nano Energy

journal homepage: www.elsevier.com/locate/nanoen

Communication

A universal synthesis strategy for single atom dispersed cobalt/metal clusters heterostructure boosting hydrogen evolution catalysis at all pH values

Shuai Yuan[a], Zonghua Pu[a], Huang Zhou[a], Jun Yu[a], Ibrahim Saana Amiinu[a], Jiawei Zhu[a], Qirui Liang[a], Jinlong Yang[a], Daping He[a,b,*], Zhiyi Hu[a,c,*], Gustaaf Van Tendeloo[c,d], Shichun Mu[a,**]

[a] State Key Laboratory of Advanced Technology for Materials Synthesis and Processing, Wuhan University of Technology, Wuhan 430070, PR China
[b] Hubei Engineering Research Center of RF-Microwave Technology and Application, Wuhan University of Technology, Wuhan 430070, PR China
[c] NRC (Nanostructure Research Centre), Wuhan University of Technology, Wuhan 430070, PR China
[d] EMAT (Electron Microscopy for Materials Science), University of Antwerp, Groenenborgerlaan 171, 2020 Antwerp, Belgium

ARTICLE INFO

Keywords:
Metal–organic frameworks
Co single atoms
Metal clusters
Hydrogen evolution reaction

ABSTRACT

The development of a stable, efficient and economic catalyst for hydrogen evolution reaction (HER) of water splitting is one of the most hopeful approaches to confront the environmental and energy crisis. A two-step method is employed to obtain metal clusters (Ru, Pt, Pd etc.) combining single cobalt atoms anchored on nitrogen-doped carbon (Ru/Pt/Pd@Co-SAs/N-C). Based on the synergistic effect between Ru clusters and single cobalt atoms, Ru@Co-SAs/N-C exhibits an outstanding HER electrocatalytic activity. Specifically, Ru@Co-SAs/N-C only needs 7 mV overpotential at 10 mA cm^{-2} in 1 M KOH solution, which is much better than commercial 20 wt% Pt/C (40 mV) catalyst. Density functional theory (DFT) calculations further reveal the synergy effect between surface Ru nanoclusters and Co-SAs/N-C toward hydrogen adsorption for HER. Additionally, Ru@Co-SAs/N-C also exhibits excellent catalytic ability and durability under acidic and neutral media. The present study opens a new avenue towards the design of metal clusters/single cobalt atoms heterostructures with outstanding performance toward HER and beyond.

1. Introduction

With the depletion of fossil fuels and increasingly serious environmental pollution, the search for clean, sustainable and eco-friendly energy sources has become a major focus of research.[1] Hydrogen is regarded as the real substitute for fossil fuels in the future because of its highest mass-specific energy density and zero carbon dioxide emission.[2] Electrochemical water splitting provides an attractive way for hydrogen production due to its simple technology, high product purity and renewability.[3] However, highly active electrocatalysts are needed for the hydrogen evolution reaction (HER).[4] Pt-based compositions, which still serve as the state-of-the-art electrocatalysts for HER, are not able to guarantee a sustainable hydrogen supply because of their high material cost and scarce reserves.[5,6] Regardless of any challenges, developing an efficient, durable, and low-cost electrocatalyst is extremely desirable for sustainable and large scale implementation of clean energy devices. So far, earth-abundant transition metals (Fe, Co, Ni, Cu, Mn, Mo and W etc.)-based materials have recently received great attention.[7–11] Nevertheless, their electrochemical activity is still far from satisfactory compared to Pt; moreover, most of them only show their best performance in acidic solutions. Additionally, the HER rate in acidic media is usually about 2–3 orders of magnitude higher than that in alkaline media. To best of our knowledge, the best catalysts for another half reaction (oxygen evolution reaction) of water splitting always work efficiently in alkaline or neutral solutions.[12,13] In this regard, probing HER catalysts with Pt-like activity suitable for alkaline media is still highly challenging, but extremely important.[14,15]

Metal-organic frameworks (MOFs) have attracted enormous attention in many applications (such as catalysis, sensing, separation, and

* Corresponding authors at: State Key Laboratory of Advanced Technology for Materials Synthesis and Processing, Wuhan University of Technology, Wuhan 430070, PR China.
** Corresponding author.
E-mail addresses: hedaping@whut.edu.cn (D. He), zhiyi.hu@whut.edu.cn (Z. Hu), msc@whut.edu.cn (S. Mu).

https://doi.org/10.1016/j.nanoen.2019.02.062
Received 21 January 2019; Received in revised form 16 February 2019; Accepted 23 February 2019
Available online 23 February 2019

gas adsorption), because of their high surface area, tunable porosity and controllable structure.[16,17] Researchers obtained different functional MOFs by varying the metal ions and organic linkers. Additionally, MOFs have been extensively reported as promising precursors/templates to develop new functional nanomaterials via carbonization/annealing or chemical treatment.[18–20] For example, Zhang et al. reported the synthesis of hollow metal oxide/hydroxide microboxes with good performance for lithium ion batteries through annealing MOFs.[18] Xia et al. reported the preparation of N-doped CNTs with excellent oxygen reduction reaction (ORR) and oxygen evolution reaction (OER) activities via pyrolysis of zeolitic imidazolate frameworks (ZIFs), a subfamily of MOFs.[21] Very recently, Li' s group reported that single atom dispersed cobalt anchored on nitrogen-doped carbon with excellent ORR activity also can be prepared by converting atomically dispersed metal nodes in-situ from ZIFs.[22] For decades, other lower-priced platinum-group metals have been studied for HER properties, because they are very similar to platinum in chemical inertia.[23] As a matter of fact, Ru as a top oxygen electrocatalytic material has attracted special attention.[24] However, in previous work, Ru was not very active in the basic media.[25] The results show that the synergistic effect of noble metals and transition metals can reduce the content of noble metals by an order of magnitude, which is the main way to prepare efficient catalysts with better cost competitiveness.[26] Therefore, the synergy of noble metals and transition metals can not only reduce the cost of materials, but also significantly improve the electrocatalytic activity resulting from the change of charge distribution and the improvement of surface properties during the formation of catalysts.[23]

In this work, we innovatively designed and synthesized metal clusters (Ru, Pt, Pd etc.) combined with single cobalt atoms anchored on nitrogen-doped carbon (Ru/Pt/Pd@Co-SAs/N-C) materials with the assistance of ZIFs. Our synthetic strategy includes two steps: (1) a pyrolysis process of predesigned bimetallic ZnCo-ZIF and the formation of single cobalt atoms anchored on nitrogen-doped carbon (Co-SAs/N-C), followed by (2) chemical reduction of the metal salt to metal clusters in the presence of Co-SAs/N-C. As electrocatalysts, for example, Ru@Co-SAs/N-C (7 mV at 10 mA cm^{-2}) shows a superior HER catalytic activity and stability in basic media in comparison with commercial Pt/C (40 mV at 10 mA cm^{-2}). Additionally, it offers an excellent catalytic performance in both acidic and neutral solutions. Density functional theory (DFT) calculations reveal that the synergistic effect between ruthenium clusters and Co-SAs/N-C toward hydrogen adsorption explains the high HER activity.

2. Materials and methods

2.1. Materials and reagent

Analytical grade Cobalt nitrate hexahydrate ($Co(NO_3)_2{\cdot}6H_2O$), Zinc nitrate hexahydrate ($Zn(NO_3)_2{\cdot}6H_2O$), Methanol, Ethanol were obtained from Sinopharm Chemical Reagents, China. 2-Methylimidazole (MeIM) was purchased from Aladdin Reagents Ltd. Ruthenium(III) chloride hydrate ($RuCl_3{\cdot}xH_2O$) and Palladium(II) chloride ($PdCl_2$) were from Shanghai Macklin Biochemical Co., Ltd. Platinic acid was from Shanghai Shiyi Chemicals Reagent Co., Ltd. The commercial Pt/C catalyst is 20% by wt. of ~3 nm Pt nanoparticles on Vulcan XC-72 carbon support. Nafion was acquired from Sigma-Aldrich. All of the chemicals used in this experiment were analytical grade and used without further purification.

2.2. Preparation of ZIF-8

In a typical procedure, $Zn(NO_3)_2{\cdot}6H_2O$ (1.118 g) was dispersed in 30 mL of methanol, which was subsequently injected into 30 mL of methanol containing 2.627 g 2-methylimidazole (MeIM) under ultrasound for 5 min at room temperature. Then, the resulting dispersion was stirred for 4 h at room temperature. The obtained product was separated by centrifugation and washed subsequently with methanol several times and finally dried at 70 °C under vacuum for overnight.

2.3. Preparation of ZIF-67

In a typical procedure, $Co(NO_3)_2{\cdot}6H_2O$ (1.092 g) was dispersed in 30 mL of methanol, which was subsequently injected into 120 mL of methanol containing 1.232 g 2-methylimidazole (MeIM) under ultrasound for 5 min at room temperature. Then, the resulting dispersion was stirred for 4 h at room temperature. The resulting ZIF-67 crystals were collected by centrifugation and washed with methanol several times and dried in vacuum at 70 °C for overnight.

2.4. Preparation of ZnCo-ZIF

In a typical procedure, $Co(NO_3)_2{\cdot}6H_2O$ (1.092 g) and $Zn(NO_3)_2{\cdot}6H_2O$ (1.118 g) were dissolved in 75 mL methanol, which was subsequently injected into 30 mL of methanol containing 1.232 g 2-methylimidazole (MeIM) under ultrasound for 5 min at room temperature. The mixed solution was then stirred at room temperature for 4 h. The as-obtained precipitates were collected by centrifugation and washed with methanol several times, and finally dried in the vacuum drying oven at 70 °C for overnight.

2.5. Preparation of N-C, Co-NPs/N-C and Co-SAs/N-C

The powder of ZIF-8, ZIF-67 and ZnCo-ZIF was placed in a tube furnace and then heated to 900 °C for 3 h under flowing Ar gas, followed by slow cooling to room temperature. The heating rate was 5 °C min^{-1}.

2.6. Preparation of $RuCl_3$@C, $RuCl_3$@N-C, $RuCl_3$@Co-NPs/N-C and $RuCl_3$ @Co-SAs/N-C

The power of XC-72, N-C, Co-NPs/N-C and Co-SAs/N-C (50 mg) was dispersed in 13 mL deionized water and stirred to form a clear solution, followed by the addition of 2 mL $RuCl_3{\cdot}xH_2O$ solution (30 mg mL^{-1}). After agitated stirring at 70 °C for 16 h, the as-obtained products were centrifuged and rinsed several times by ethanol, and finally dried in vacuum at 70 °C for overnight.

2.7. Preparation of Ru-Co NPs@N-C

ZnCo-ZIF (100 mg) was dissolved in 100 mL water, followed by the addition of 2 mL $RuCl_3{\cdot}xH_2O$ solution (30 mg mL^{-1}). After agitated stirring for 4 h, the as-obtained products were centrifuged and rinsed several times by ethanol, and finally dried in vacuum at 70 °C for overnight. Subsequently, the samples were heated to 900 °C for 3 h at a heating speed of 5 °C min^{-1} under flowing Ar gas. After cooled to room temperature, Ru-Co NPs@N-C was obtained.

2.8. Preparation of H_2PtCl_6@Co-SAs/N-C

Co-SAs/N-C (50 mg) was dispersed in 10 mL deionized water and stirred to form a clear solution, followed by the addition of 5 mL H_2PtCl_6 solution (30 mg mL^{-1}). After agitated stirring at 70 °C for 16 h, the as-obtained products were centrifuged and rinsed several times by ethanol, and finally dried in vacuum at 70 °C for overnight.

2.9. Preparation of $PdCl_2$@Co-SAs/N-C

The power of Co-SAs/N-C (50 mg) was dispersed in 11.58 mL deionized water and stirred to form a clear solution, followed by the addition of 1.71 mL $PdCl_2$ acid solution (30 mg mL^{-1}) and 1.71 mL KOH solution (1 mol L^{-1}). After agitated stirring at 70 °C for 16 h, the as-obtained product was centrifuged and rinsed several times by ethanol, and

finally dried in vacuum at 70 °C for overnight.

2.10. Preparation of Ru@C, Ru@N-C, Ru@Co-NPs/N-C and Ru@Co-SAs/N-C

Ru@C, Ru@N-C, Ru@Co-NPs/N-C and Ru@Co-SAs/N-C products were obtained by the pyrolysis of $RuCl_3$@C, $RuCl_3$@N-C, $RuCl_3$@Co-NPs/N-C and $RuCl_3$@Co-SAs/N-C at 125 °C for 1 h under Ar atmosphere, followed by slow cooling to room temperature.

2.11. Preparation of Pt@Co-SAs/N-C

Pt@Co-SAs/N-C products were obtained by the pyrolysis of H_2PtCl_6@Co-SAs/N-C at 400 °C for 1 h under Ar atmosphere, followed by slow cooling to room temperature.

2.12. Preparation of Pd@Co-SAs/N-C

Pd@Co-SAs/N-C products were obtained by the pyrolysis of $PdCl_2$@Co-SAs/N-C at 200 °C for 1 h under Ar atmosphere, followed by slow cooling to room temperature.

2.13. Characterization

Transmission electron microscopy (TEM) was performed on a HITACHI H-8100 electron microscopy operated at 200 kV. High Angle Annular Dark Field Scanning Transmission Electron Microscopy (HAADF-STEM) and Energy Dispersive X-ray Spectroscopy (EDX) were performed on a FEI Titan Themis microscope fitted with aberration-correctors for the imaging lens and the probe forming lens, Super-X EDX system, operated at 300 kV. XRD patterns were collected on a Bruker D8 Advance X-ray diffractometer with a Cu Kα radiation. XPS measurements were performed on a Thermo Fischer ESCALAB 250Xi spectrometer. SEM measurements were carried out on a XL30 ESEM FEG scanning electron microscope at an accelerating voltage of 20 kV. N_2 adsorption/desorption isotherms and pore size distributions were measured with ASAP 2020 M at 77 K. BET surface area was recorded by N_2 adsorption-desorption isotherms with a Quantachrome NOVA 4200e. ICP-AES analysis was performed on Optima Prodigy 7 (LEEMAN LABS Ltd., USA). The ICP-AES elemental analyses were performed to obtain the Co and Ru amount in the Ru@Co-SAs/N-C. Specifically, 2.0 mg Ru@Co-SAs/N-C was placed in a 50 mL Teflon-lined autoclave, and 5.0 mL HNO_3, 1.0 mL HCl and 1.0 mL HF were then added. The Teflon-lined autoclave was subsequently sealed and treated at 200 °C for 5 h. After cooling to room temperature, the solution in the Teflon-lined autoclave was diluted with water to 25 mL in a volumetric flask. Using the ICP-AES elemental analyses, the concentration of Co and Ru ions in the solution was measured.

2.14. Electrochemical measurements

All electrochemical measurements were performed on an Autolab PG 302 N electrochemical analyzer in a standard 3-electrode with 2-compartment cell. The alkaline (1 M KOH) electrochemical measurements were performed using a Hg/HgO as the reference electrode. The acidic (0.5 M H_2SO_4) electrochemical measurements were performed using a Ag/AgCl as the reference electrode. The neutral (1 M PBS) electrochemical measurements were performed using a saturated calomel electrode (SCE) as the reference electrode. A graphite plate was used as the counter electrode in all measurements. Polarization data were obtained at a scan rate of 5 mV s^{-1}. In all measurements, the reference electrode was calibrated with respect to reversible hydrogen electrode (RHE). The calibration was performed in the high purity hydrogen saturated electrolyte with a Pt wire as the working electrode. The current-voltage was run at a scan rate of 2 mV s^{-1}, and the average of the two potentials at which the current crossed zero was taken to be the thermodynamic potential for the hydrogen electrode reactions. To prepare the catalyst ink, 5 mg catalyst powder was ultrasonically dispersed in 500 μL mixed liquor (20 μL Nafion ionomer solution, 432 μL isopropanol and 48 μL deionized water). Then 2 μL of the dispersion was loaded onto a glassy carbon electrode with 3 mm diameter (loading 0.285 mg cm^{-2}). The obtained HER polarization curves were IR-compensated according to the following equation: $E_c = E_m - IR$ (where E_c is the IR-compensated potential, E_m is the experimentally measured potential, R is the solution resistance). The long-term stability was tested by a potentiation method at fixed potentials. For Faradic efficiency test, the Ru@Co-SAs/N-C was loading on carbon cloth with a loading weight of 1.0 mg cm^{-2}. The Faradic yield is defined as the ratio of the amount of experimentally determined hydrogen to that of the theoretically expected hydrogen. The H_2 was collected via the water drainage method. A constant potential was applied on the electrode and the volume of evolved gases was recorded synchronously. The Faradic yield was then calculated as the ratio of measured amount of H_2 and theoretical amount of H_2 (based on Faraday's law).

3. Result and discussion

The synthetic route of Ru/Pt/Pd@Co-SAs/N-C is illustrated in Fig. 1**a**. ZnCo-ZIF is first synthesized. Scanning electron microscopy (SEM) (Fig. S1a) and transmission electron microscopy (TEM) (Fig. 1**b** and Fig. S1d) reveal that the ZnCo-ZIF shows a well-defined rhombic dodecahedral shape with smooth surfaces and a uniform size distribution. Then, the Co-SAs/N-C with Co-N_x single sites is obtained after carbonization the ZnCo-ZIF precursor at 900 °C in Ar atmosphere. SEM (Fig. S1b), TEM (Fig. 1**c** and Fig. S1e) and high-angle annular dark-field scanning transmission electron microscopy (HAADF-STEM) (Fig. 1**d** and Fig. S2) observations indicate that the as-obtained Co-SAs/N-C preserves the rhombic dodecahedral morphology well and possesses abundant Co single atoms (assigned to bright dots on nitrogen-doped porous carbon in Fig. 1**d**), which is in great agreement with previous reports.[18] Finally, Ru/Pt/Pd@Co-SAs/N-C is obtained through chemical reduction $RuCl_3{\cdot}xH_2O/H_2PtCl_6/PdCl_2$ to Ru/Pt/Pd clusters in the presence of Co-SAs/N-C. As shown in Fig. 1**e-g** and Fig. S3, from TEM images, tiny metal clusters with a size of 1–2 nm can be observed with a good dispersion on Ru/Pt/Pd@Co-SAs/N-C.

HAADF-STEM image (Fig. 2**a**) shows that the Ru@Co-SAs/N-C structure maintains its initial rhombic dodecahedral shape with a mean diameter of about 200 nm. High resolution HAADF-STEM (Fig. 2**c**) and STEM energy dispersive X-ray (STEM-EDX) elemental analysis (Fig. 2**d** and Fig. S4) clearly reveal that most of the Ru clusters are homogeneously distributed on the outside surface of the Ru@Co-SAs/N-C, which guarantees the full use of the active site of Ru clusters, and thereby stimulating the hydrogen generation from water. Also, EDX mapping in Fig. 2**d** and HAADF-STEM image in Fig. 2**b** and Fig. S5 further reveal the Co single atoms are still uniform monodispersed (the bright dots assigned to Co atoms were circled in yellow for better observation). The inductively coupled plasma atomic emissions spectrometry (ICP-AES) shows the ratio of Co(wt%): Ru (wt%) is about 0.157 (Table S2), indicating the much less of Co compared to Ru in Co-SAs/N-C. Very importantly, the developed strategy is also effective in the synthesis of other metal clusters anchoring on Co-SAs/N-C (e.g. Pt@Co-SAs/N-C and Pd@Co-SAs/N-C). The mass percent of Pt/Pd in Pt/Pd@Co-SAs/N-C are 6.96% and 4.09% (Table S3). The typical HAADF-STEM images and corresponding EDX elemental maps are shown in Fig. 2**e, f**.

XRD pattern of Co-SAs/N-C and Ru@Co-SAs/N-C (Fig. 2**g**) further exhibit that there are no characteristic signals of Co and Ru, indicating the presence of Co and Ru are single atoms or clusters. The N_2 adsorption–desorption isotherms reveal that Co-SAs/N-C is composed of both micro- and meso-pores and has a high Brunauer–Emmett–Teller (BET) surface area of 742.02 m^2 g^{-1}. However, when in-situ chemical reduction $RuCl_3{\cdot}xH_2O$ to Ru clusters in the presence of Co-SAs/N-C, the

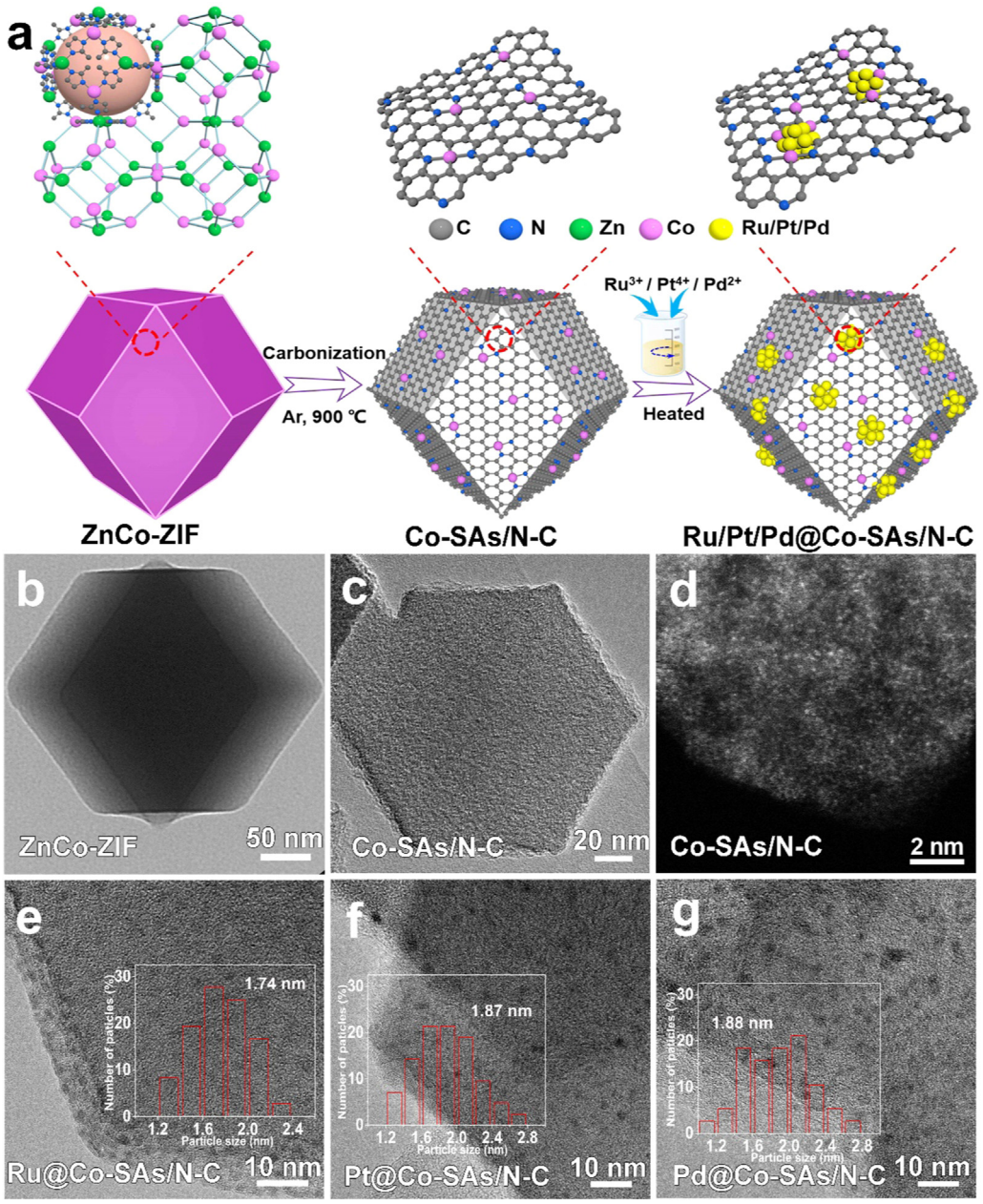

Fig. 1. Synthetic mechanism and electron microscopy characterization. (a) Synthesis schematic diagram of the Ru/Pt/Pd@Co-SAs/N-C. TEM images of (b) ZnCo-ZIF, (c) Co-SAs/N-C, (d) HAADF-STEM image of Co-SAs/N-C, TEM images of (e) Ru@Co-SAs/N-C, (f) Pt@Co-SAs/N-C, (g) Pd@Co-SAs/N-C (Inset: Size distribution of (e) Ru@Co-SAs/N-C, (f) Pt@Co-SAs/N-C, (g) Pd@Co-SAs/N-C).

BET surface area for Ru@Co-SAs/N-C (262.29 $m^2 g^{-1}$) decreases (Fig. S8 and Table S4). This may be attributed to the small particle size of the Ru clusters that leads to entering into the micro- and meso-pores of Co-SAs/N-C. This specific structure may contribute to the high stability of Ru@Co-SAs/N-C. Besides, by the X-ray photoelectron spectroscopy (XPS) measurements, the binding energy of the Co $2p_{3/2}$ peak in Ru@Co-SAs/N-C is 779.8 eV, which is higher than that reported for Co^0 (778.1–778.8 eV)[27,28] and lower than that for Co^{2+} (780.9 eV),[28] revealing the ionic $Co^{\delta+}$ ($0 < \delta < 2$) nature of Co in Ru@Co-SAs/N-C (Fig. S9a). For Ru $3d_{5/2}$, the binding energy peak at 280.4 eV is similar to that of reported for Ru^0 (280.0–280.5 eV),[29,30] suggesting the bulk Ru nature in Ru@Co-SAs/N-C (Fig. 2**j**). The N 1s XPS spectrum (Fig. S9b**)** reveals that three typical N status including pyridinic N (pyri-N, 397.6 eV), graphitic N (grap-N, 398.8 eV) and pyrrolic N (pyrr-N, 399.8 eV) are dominant in the Ru@Co-SAs/N-C.[22,31] In addition, control samples of Ru@C, Ru@N-C and Ru@Co-NPs/N-C were also analysed by means of HAADF-TEM, XPS and XRD (Fig. S10-S18). Fig. S10 shows that the Co and Zn absent cause the formation of small Ru nanoparticles of about 2–3 nm. Also, the EDX mapping collaboratively supports that the Ru nanoparticles distributes inhomogenously in the whole composite. Aberration corrected HAADF-STEM (Fig. S11) revealed that isolated light spots are fastened homogenously on the N-C matrix. These sites may be attributed to the Ru particles. In addition, the Zn^{2+} nodes aren't replaced by Co^{2+} ions, the mobile sub-nano Ru particles can't tend to migrate and assemble coordinate with Co nodes. As illustrated in Fig. S12, there are large nanoparticles observed on the N-C support, indicating the over-growth of Co nanoparticles can't be depressed by the ZIF-67. In addition, it is believed that the Ru clusters distribute on rhombic dodecahedral polyhedrons, and not only on the surface. X-ray photoelectron spectroscopy (XPS) of Ru@Co-SAs/N-C also affirms that the catalyst is composed of C, N, O, Ru and Co elements (Fig. S13a). From the Fig. S13b **and c**, the shfit of Ru and Co

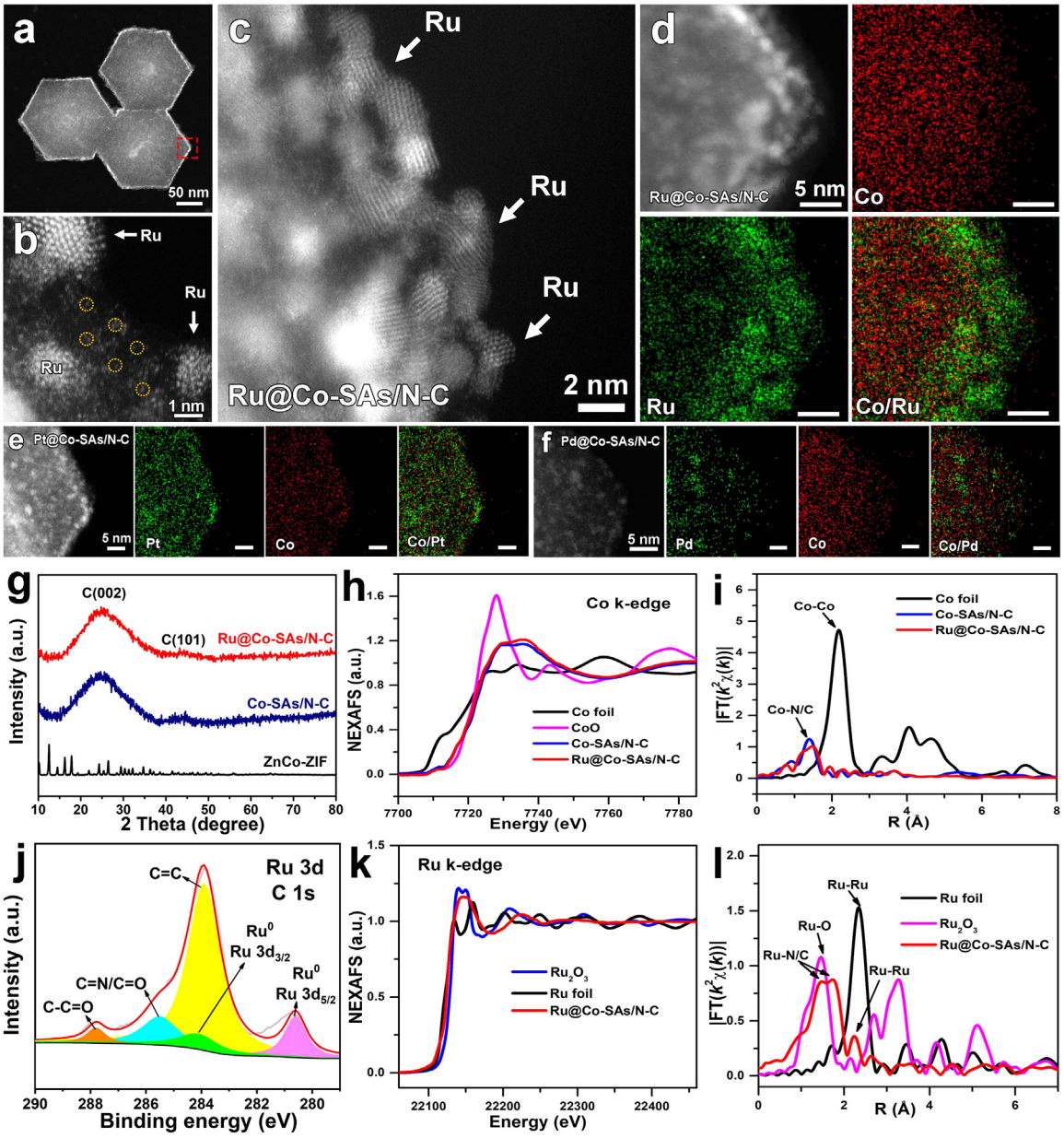

Fig. 2. Electron microscopy characterization and chemical structure of Ru/Pt/Pd@Co-SAs/N-C. (a) HAADF-STEM image at low magnification of Ru@Co-SAs/N-C; (b) enlarged HAADF-STEM image of Ru@Co-SAs/N-C; (c) HAADF-STEM image at high magnification of the area indicated by red box in a; HAADF-STEM images of (d) Ru@Co-SAs/N-C, (e) Pt@Co-SAs/N-C, (f) Pd@Co-SAs/N-C respectively, and corresponding EDX elemental maps: Co (red) and Ru/Pt/Pd (green); (g) XRD patterns of as-prepared Ru@Co-SAs/N-C, Co-SAs/N-C and ZnCo-ZIF. (h) Co K-edge XANES spectra and (i) the k^2-weighted $\chi(k)$-function of the EXAFS spectra. (j) High-resolution XPS spectra of C 1s and Ru 3d of Ru@Co-SAs/N-C composite. (k) Ru K-edge XANES spectra and (l) the k^2-weighted $\chi(k)$-function of the EXAFS spectra.

peaks indicates that Ru and Co exist in different forms in the Ru@Co-SAs/N-C, Ru@Co-NPs/N-C and Co-SAs/N-C. X-ray photoelectron spectroscopy (XPS) of Ru@Co-NPs/N-C also affirms that the catalyst is composed of C, N, O, Ru and Co elements (Fig. S17). As shown in Fig. S17a, there is no Ru $3d_{5/2}$ signal, while the subpeaks located at 284.5, 285.5 and 287 eV are corresponding to the C=C, C=N/C=O and C-C=O, respectively (Fig. S17d). The high resolution Co 2p XPS spectrum (Fig. S17b) exhibits two peaks at 779.9 and 796.2 eV, which are ascribed to metallic Co $2p_{3/2}$ and $2p_{1/2}$, respectively. The crystallized Co phase prevailed, as confirmed by the appearance of Co NPs. The N 1 s XPS spectrum (Fig. S17c) reveals three typical N status including pyridinic N (pyri-N, 397.6 eV), graphitic N (grap-N, 398.2 eV) and pyrrolic N (pyrr-N, 399.8 eV), indicating the successful incorporation of N into carbon layers. A set of well-defined face-centered cubic Co peaks appear for pyrolyzed ZIF-67 (Fig. S18). Incontrast, utilizing ZnCo-ZIF as a precursor, no peaks characteristic of Co crystals emerged. Similarly, XRD patterns of Ru@Co-SAs/N-C, Ru@C, Ru@Co-NPs/N-C and Ru@N-C shows no clearcrystalline Ru peaks.

The structure of the Co-SAs/N-C and Ru@Co-SAs/N-C were further investigated by the X-ray absorption near-edge structure (XANES) and the extended X-ray absorption fine structure (EXAFS). As shown in Fig. 2**h**, the position of the peaks of Co k-edge for Co-SAs/N-C and Ru@Co-SAs/N-C are both located between those of Co foil and CoO, indicating that the valence state of Co SAs is situated between that of Co^0 and Co^{II}. This observation result agrees well with above XPS measurements. Further structural information can be obtained from the EXAFS. As shown in Fig. 2**i**, the similar intensity of the peak at 1.5 Å, which is lower than that of Co foil (2.15 Å) and can be assigned to the first shell of Co-N/C scattering, demonstrating that the Co atoms are atomically dispersed in Co-SAs/N-C and Ru@Co-SAs/N-C.[22] For

Ru@Co-SAs/N-C, the Ru K-edge XANES spectrum is similar to that of Ru foil, indicating the metal state of Ru (Fig. 2**k**). Ru@Co-SAs/N-C mainly showed the Ru-N and Ru-C coordination at the peaks of 1.46 and 1.65 Å, respectively. A weaker peak attributed to Ru-Ru bond is also observed at 2.23 Å, which is much lower than that of bulky Ru (2.34 Å) (XAFS spectra of the Co-SAs/N-C and Ru@Co-SAs/N-C catalysts at the Co and K-edge are shown in Fig. S19). This phenomenon is due to the surface contraction in cluster structure, agreeing well with the previously reported results.[32]

The HER electrocatalytic activity of Ru@Co-SAs/N-C, Pt@Co-SAs/N-C and Pd@Co-SAs/N-C was first probed in a typical three-electrode electrochemical system with 1 M KOH electrolyte at room temperature. As shown in Fig. S20, the catalytic performance in sequence is Pt@Co-SAs/N-C > Ru@Co-SAs/N-C > Pd@Co-SAs/N-C. As an exsample, here, Ru@Co-SAs/N-C was selected for further study. As shown in Fig. S21, the dependence of HER rate on the loading amount of the Ru@Co-SAs/N-C can be observed. The optimal loading is 0.285 mg cm^{-2}. When the loading weight is higher, a lower catalytic performance is obtained. For comparison, the electrocatalytic actives of Ru@N-C, Ru@Co-NPs/N-C, Ru@C, Co-SAs/N-C, commercial Pt/C (20 wt%) and Ru-Co NPs@N-C (synthesized by a one-step method. The detailed synthesize process is in the Experimental section.) were also tested under the same conditions. As depicted in Fig. 3**a**, Co-SAs/N-C displays a poor HER activity, while Ru@Co-SAs/N-C displays outstanding HER catalytic activities with 0 mV onset overpotential (η_{onset}). In addition, to drive the current density of 10 mA cm^{-2} (j_{10}), the Ru@Co-SAs/N-C catalyst only needs an overpotential of 7 mV (14 mV without IR correction, Fig. S22) with IR correction. This value is much lower than that of Ru@Co-NPs/N-C (j_{10} = 107 mV), Ru@N-C (j_{10} = 134 mV), Ru@C (j_{10} = 164 mV), Co-SAs/N-C (j_{10} = 223 mV) and Ru-Co NPs@N-C (j_{10} = 95 mV, Fig. S23c); and even lower than the commercial Pt/C (j_{10} = 40 mV) (Fig. 3**b**). More importantly, this is the lowest overpotential value of all recently reported catalysts (Table S5). In addition, as illustrated in Fig. S24, the HER mass activity of Ru@Co-SAs/N-C is also much higher than that of Ru@Co-NPs/N-C, Ru@N-C and Ru@C. Fig. 3**c** further displays that the Tafel slope for Ru@Co-SAs/N-C is ~30 mV dec^{-1}, much smaller than the value of 46 mV dec^{-1} for commercial Pt/C and various representative catalysts reported recently (Table S5).

Fig. 3**d** shows that the HER polarization curve of Ru@Co-SAs/N-C after 3000 CV cycles almost overlaps with the initial one. Moreover, the inset of Fig. 3**d** exhibits the chronoamperometry curves for Ru@Co-SAs/N-C and commercial Pt/C at fixed overpotentials. Ru@Co-SAs/N-C shows the best durability with a negligible degradation of the current density even after 24 h, whereas the current density of commercial Pt/C degrades much with time. The excellent stability of Ru@Co-SAs/N-C can be related to the Co-SAs/N-C anchoring the Ru clusters, and therefore protecting the Ru clusters from corrosion and aggregation. Furthermore, TEM and XPS were employed to demonstrate the strong stability of the Ru@Co-SAs/N-C catalyst after 3000 cycles. Relevant TEM observations from before and after 3000 cycles of Ru@Co-SAs/N-C certify that the morphology is hardly altered (Fig. S25). In addition, the similarity of high-resolution Ru 3d, C 1s, N 1s, Co 2p and O 1s XPS spectra (Fig. S26) of the fresh and post-HER Ru@Co-SAs/N-C samples also confirmed the retention of the electrocatalysts in terms of

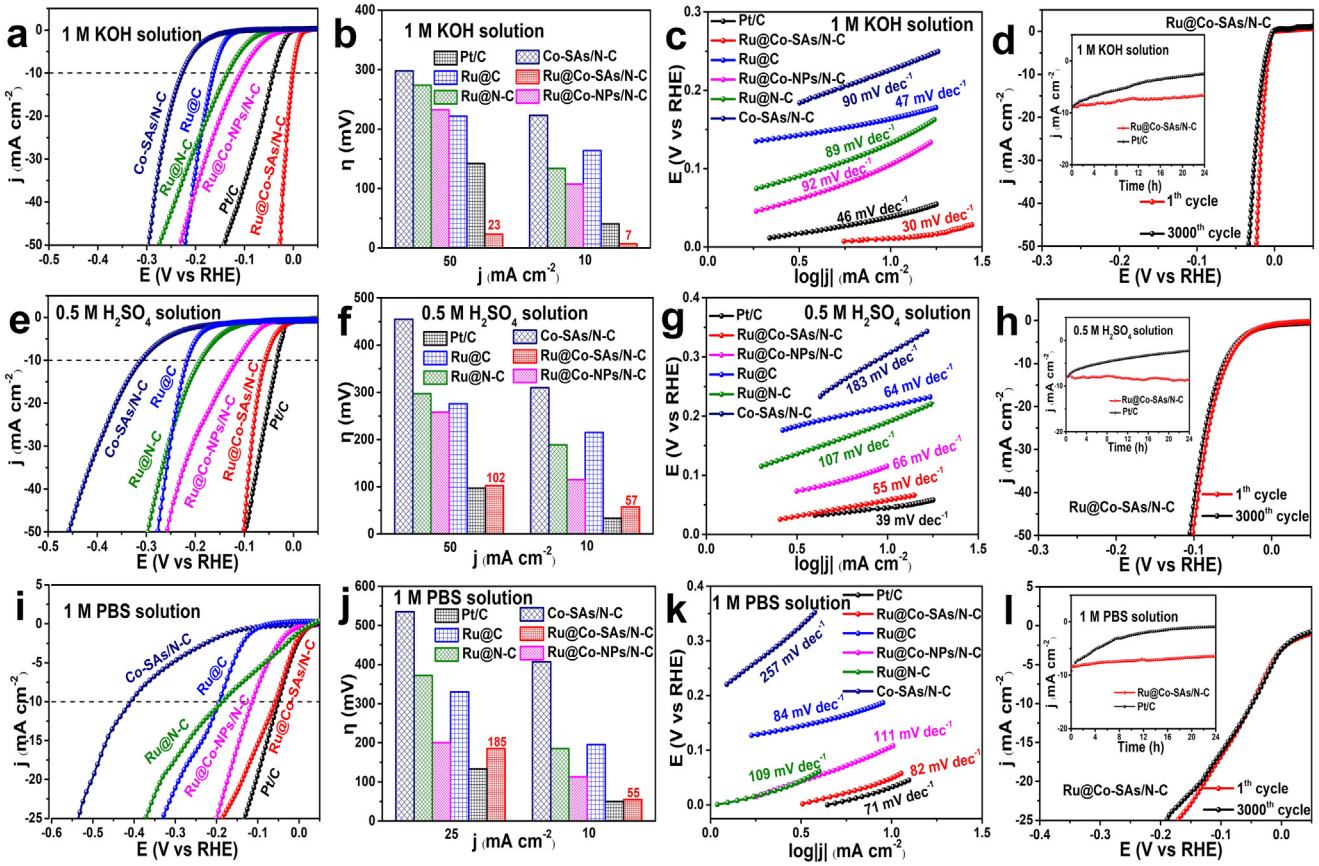

Fig. 3. Electrocatalytic activities of Ru@Co-SAs/N-C in alkaline media, acidic and neutral conditions. HER polarization curves of Ru@Co-SAs/N-C, Pt/C, Ru@C, Ru@Co-NPs/N-C, Ru@N-C and Co-SAs/N-C in (a) 1 M KOH, (e) 0.5 M H_2SO_4 and (i) 1 M PBS at a scan rate of 5 mV s^{-1}. Overpotentials at corresponding j (10/25/50 mA cm^{-2}) for Ru@Co-SAs/N-C, Pt/C, Ru@C, Ru@Co-NPs/N-C, Ru@N-C and Co-SAs/N-C in (b) 1 M KOH and (f) 0.5 M H_2SO_4, and (j) 1 M PBS. (c, g and k) Corresponding Tafel plots for Ru@Co-SAs/N-C, Pt/C, Ru@C, Ru@Co-NPs/N-C, Ru@N-C and Co-SAs/N-C. Polarization curves recorded for Ru@Co-SAs/N-C before and after 3000 CV cycles in (d) 1 M KOH, (h) 0.5 M H_2SO_4 and (l) 1 M PBS (Inset: Time-dependent current density curve of the Ru@Co-SAs/N-C and Pt/C in (d) 1 M KOH, (h) 0.5 M H_2SO_4 and (l) 1 M PBS).

morphology and composition, corroborating its superior robustness for HER electrocatalysis. These results demonstrate the strong stability of Ru@Co-SAs/N-C toward HER in alkaline media.

Fig. 3**e, i** further show that Ru@Co-SAs/N-C reaches a current density of 10 mA cm^{-2} at overpotentials of only 57 and 55 V in 0.5 M H_2SO_4 and 1 M PBS electrolytes, and the corresponding Tafel slopes are 55 and 82 mV dec^{-1}, respectively (Fig. 3**g**, **k**). Such impressive low overpotentials and low Tafel slopes can compare with most of the recently developed noble metals, non-noble metals and nonmetallic HER electrocatalysts (Table S5). In addition, the Tafel slope of Ru@Co-SAs/N-C of 55 mV dec^{-1} in acidic solutions, suggests that Ru@Co-SAs/N-C primarily goes through a Volmer−Heyrovsky HER mechanism (Fig. S27).[33] Notably, the HER activity of Ru@Co-SAs/N-C in acidic solution is even lower than that in alkaline electrolyte, suggests that Ru is able to efficiently dissociate water to promote subsequent hydrogen adsorption and recombination. This result is also consistent with recent reported work.[33,34] Furthermore, after 3000 CV cycles in both acidic and neutral solutions, the polarization curve shows almost negligible degradation (Fig. 3**h**, **l**). The insets of Fig. 3**h** and **l** show that Ru@Co-SAs/N-C maintained durability after testing for 24 h. The hydrogen yield catalyzed by Ru@Co-SAs/N-C indicates nearly 100% faradic yield for hydrogen generation in alkline, acidic and neutral (Fig. S28).[35] On the basis of above data (Fig. 3 and Fig. S29-S30), we can conclude that Ru/Pt/Pd@Co-SAs/N-C are an active and stable electrocatalyst for HER over a wide pH range.

DFT analysis was used to advance our understanding of the origin of the high catalytic activity toward HER (computation details are given in Supporting information). Due to the Gibbs free energy (ΔG_{H^*}) for the chemisorption of hydrogen is recognized to have a strong correlation with the HER activity, we first computed the Gibbs free energy (ΔG_{H^*}) of simulated catalyst samples for the respective metal-carbon phases and the composite structure to determine the contribution of the metallic species to the overall catalytic performance. As shown in Fig. S31a, the N-doped-carbon (N-C) framework displays a $|\Delta G_{H^*}|$ value of ~0.523 eV, while the Co-N_x-C coupling framework with Co atoms doping shows a lower free energy (−0.287 eV), in agreement with previous literatures.[36,37] The relatively weak H* adsorption activity of N-C compared to Co-SAs/N-C is indicative that the high HER activity of Co-SAs/N-C catalysts arises from the metal-N coupling sites rather than the N-C sites. Interestingly, the Ru@Co-SAs/N-C composite system displays the lowest $|\Delta G_{H^*}|$ value of ~0.107 eV which is significantly closer to the optimum thermodynamic zero value. This demonstrates that intermediate H* binds neither too weakly nor too strongly to the Ru site of the Ru@Co-SAs/N-C system, which is highly favorable for promoting electrocatalytic HER activity. Also, to better understand the HER mechanism, we explored the H_2O dissociation path. As shown in Fig. S31b, the N-C framework exhibits a poor adsorption kinetics toward OH* intermediates. Such a relatively high adsorption activity is unfavorable for effectively catalyzing intermediate H* generation by H_2O dissociation, thereby leading to a sluggish HER kinetic process. However, by integrating Co atoms into the carbon framework, the resultant Co-N_x-C coupling structure exhibits reduction of the energy barrier, indicating that the Co-N coupling can enhance the kinetic activity toward HER. The Ru@Co-SAs/N-C composite displays the most significantly reduced energy barrier with the lowest adsorption energy of the intermediate species. This further suggests that the synergy between surface Ru nanoclusters and Co-SAs/N-C can efficiently stimulate cleavage of the HO–H bonds of H_2O to generate the required H* intermediate species, which then adsorb at active Ru sites to boost the HER kinetic process. Furthermore, the electron density difference (EDD) was probed to visualize how the charge density changes upon interaction with H* (Fig. S31c**, d**).[30,38] The charge density distribution (Fig. S33) displays an enhanced hybridization of the Ru-d and Co-d orbitals which is favorable for boosting interactions of dissociated intermediates at the Ru-Co coupling centers. The two-dimensional EDD mapping (Fig. S31c, **d**) shows that the interaction of adsorbed H* is more favorable toward Ru compared to the Co, N and C centers. This is evidenced by the high electron depletion from Ru atoms (blue isosurface) toward electron enrichment, by transfer, to enhance the adsorption of intermediate H* species. In addition, the unique nanostructure of the Co-SAs/N-C supported Ru nanoclusters not only avoids aggregation of the Ru nanoclusters, but also guarantees the high activity and strong durability of the catalyst during long-term operation. Furthermore, the collaborative effect between Ru nanoclusters and Co-SAs/N-C toward hydrogen adsorption can explain why Ru@Co-SAs/N-C has such high HER activity.

4. Conclusion

We successfully prepared a series of metal clusters combined with single cobalt atoms anchored on nitrogen-doped carbon. As HER catalysts, the prepared Ru@Co-SAs/N-C exhibits outstanding catalytic ability and durability all pH values. The DFT calculations validate that the synergistic effect between Ru clusters and Co-SAs/N-C is responsible for the high yields and outstanding HER performance. This work opens new opportunities for the preparation of metal clusters combined with single cobalt atoms, beneficial for electrocatalytic applications.

Acknowledgements

S.Y., Z.P. and H.Z. contributed equally to this work. This work was financed by the National Natural Science Foundation of China (Grant No. 51372186, 51672204, 51701146) and the Fundamental Research Funds for the Central Universities (WUT: 2017III055, 2018III039GX, 2018IVA095). We express heartfelt thanks to Prof. Gaoke Zhang for the supply of computational resources in the School of Resources and Environmental Engineering, Wuhan University of Technology.

Appendix A. Supporting information

Supplementary data associated with this article can be found in the online version at doi:10.1016/j.nanoen.2019.02.062.

References

[1] S. Chu, A. Majumdar, Opportunities and challenges for a sustainable energy future, Nature 488 (2012) 294.
[2] J.A. Turner, Sustainable hydrogen production, Science 305 (2004) 972.
[3] Z. Yao, J. Yan, J. Mietek, S.Z. Qiao, Advancing the electrochemistry of the hydrogen-evolution reaction through combining experiment and theory, Angew. Chem. Int. Ed. 54 (2015) 52.
[4] P. Shengjie, L. Linlin, H. Xiaopeng, S. Wenping, S. Madhavi, S.G. Mhaisalkar, C. Fangyi, Y. Qingyu, C. Jun, R. Seeram, Cobalt sulfide nanosheet/graphene/carbon nanotube nanocomposites as flexible electrodes for hydrogen evolution, Angew. Chem. Int. Ed. 126 (2014) 12802.
[5] H. Yin, S. Zhao, K. Zhao, A. Muqsit, H. Tang, L. Chang, H. Zhao, Y. Gao, Z. Tang, Ultrathin platinum nanowires grown on single-layered nickel hydroxide with high hydrogen evolution activity, Nat. Commun. 6 (2015) 6430.
[6] H.B. Gray, Powering the planet with solar fuel, Nat. Chem. 1 (2009) 7.
[7] H.B. Wu, B.Y. Xia, L. Yu, X.Y. Yu, X.W. Lou, Porous molybdenum carbide nano-octahedrons synthesized via confined carburization in metal-organic frameworks for efficient hydrogen production, Nat. Commun. 6 (2015) 6512.
[8] H. Yan, C. Tian, L. Wang, A. Wu, M. Meng, L. Zhao, H. Fu, Phosphorus-modified tungsten nitride/reduced graphene oxide as a high-performance, non-noble-metal electrocatalyst for the hydrogen evolution reaction, Angew. Chem. Int. Ed. 127 (2015) 6423.
[9] J. Wang, F. Xu, H. Jin, Y. Chen, Y. Wang, Non-noble metal-based carbon composites in hydrogen evolution reaction: fundamentals to applications, Adv. Mater. 29 (2017) 1605838.
[10] X. Zou, Y. Zhang, Noble metal-free hydrogen evolution catalysts for water splitting, Chem. Soc. Rev. 44 (2015) 5148.
[11] J. Wang, Z. Huang, W. Liu, C.R. Chang, H. Tang, Z. Li, W. Chen, C. Jia, T. Yao, S. Wei, Design of N-coordinated dual-metal sites: a stable and active Pt-free catalyst for acidic oxygen reduction reaction, J. Am. Chem. Soc. 139 (2017) 17281–17284.
[12] M.G. Walter, E.L. Warren, J.R. Mckone, S.W. Boettcher, Q. Mi, E.A. Santori, N.S. Lewis, Solar water splitting cells, Chem. Rev. 110 (2010) 6446.
[13] Y. Zheng, Y. Jiao, Y. Zhu, L.H. Li, Y. Han, Y. Chen, M. Jaroniec, S.Z. Qiao, High electrocatalytic hydrogen evolution activity of an anomalous ruthenium catalyst, J.

Am. Chem. Soc. 138 (2016) 16174.
[14] Y. Meidan, G. Jiaojiao, L. Yuekun, L. Changjian, L. Zhiqun, High-efficiency photoelectrocatalytic hydrogen generation enabled by palladium quantum dots-sensitized TiO_2 nanotube arrays, J. Am. Chem. Soc. 134 (2012) 15720.
[15] S. Lan, W. Zhi, S. Xiang, J. Yu, Y. Wang, C. Lin, Z. Lin, High-efficiency photoelectrochemical hydrogen generation enabled by p-type semiconductor nanoparticle-decorated n-type nanotube arrays, RSC Adv. 7 (2017) 17551.
[16] H. Furukawa, K. Cordova, M. O'Keeffe, M.O. Yaghi, The chemistry and applications of metal-organic frameworks, Science 341 (2013) 1230444.
[17] S. Norbert, B. Shyam, Synthesis of metal-organic frameworks (MOFs): routes to various MOF topologies, morphologies, and composites, Chem. Soc. 43 (2012) 933.
[18] L. Zhang, H.B. Wu, X.W. Lou, Metal-organic-frameworks-derived general formation of hollow structures with high complexity, J. Am. Chem. Soc. 135 (2013) 10664.
[19] L. Zhang, H.B. Wu, S. Madhavi, H.H. Hng, X.W. Lou, Formation of Fe_2O_3 microboxes with hierarchical shell structures from metal-organic frameworks and their lithium storage properties, J. Am. Chem. Soc. 134 (2012) 17388.
[20] Y. Cheng, J. Guo, H. Yan, Z. Liao, Z. Xiang, Ultrastable hydrogen evolution electrocatalyst derived from phosphide postmodified metal-organic frameworks, Nano Energy 35 (2017) 115.
[21] B.Y. Xia, Y. Yan, N. Li, H.B. Wu, X.W. Lou, X. Wang, A metal–organic framework-derived bifunctional oxygen electrocatalyst, Nat. Energy 1 (2016) 15006.
[22] P. Yin, T. Yao, Y. Wu, L. Zheng, Y. Lin, W. Liu, H. Ju, J. Zhu, X. Hong, Z. Deng, G. Zhou, S. Wei, Y. Li, Single cobalt atoms with precise N-coordination as superior oxygen reduction reaction catalysts, Angew. Chem. Int. Ed. 55 (2016) 10800.
[23] J. Chen, G. Xia, P. Jiang, Y. Yang, R. Li, R. Shi, J. Su, Q. Chen, Active and durable hydrogen evolution reaction catalyst derived from Pd-doped metal-organic frameworks, ACS Appl. Mater. Interfaces 8 (2016) 13378.
[24] J. Yan, Z. Yao, J. Mietek, Q.S. Zhang, Design of electrocatalysts for oxygen- and hydrogen-involving energy conversion reactions, Chem. Soc. Rev. 46 (2015) 2060.
[25] B. Pierozynski, T. Mikolajczyk, I.M. Kowalski, Hydrogen evolution at catalytically-modified nickel foam in alkaline solution, J. Power Sources 271 (2014) 231.
[26] J. Su, Y. Yang, G. Xia, J. Chen, P. Jiang, Q. Chen, Ruthenium-cobalt nanoalloys encapsulated in nitrogen-doped graphene as active electrocatalysts for producing hydrogen in alkaline media, Nat. Commun. 8 (2017) 14969.
[27] Y. Pan, R. Lin, Y. Chen, S. Liu, W. Zhu, X. Cao, W. Chen, K. Wu, W.C. Cheong, Y. Wang, Design of single-atom Co-N5 catalytic site: a robust electrocatalyst for CO_2 Reduction with nearly 100% CO selectivity and remarkable stability, J. Am. Chem. Soc. 140 (2018) 4218.
[28] M. Zhang, Q. Dai, H. Zheng, M. Chen, L. Dai, Novel MOF-derived, Co@N-C bifunctional catalysts for highly efficient Zn–air batteries and water splitting, Adv. Mater. 30 (2018) 1705431.
[29] T. Bhowmik, M.K. Kundu, S. Barman, Growth of one-dimensional RuO_2 nanowires on g-carbon nitride: an active and stable bifunctional electrocatalyst for hydrogen and oxygen evolution reactions at all pH values, ACS Appl. Mater. Interfaces 8 (2016) 28678.
[30] U. Joshi, S. Malkhandi, Y. Ren, T.L. Tan, S.Y. Chiam, B.S. Yeo, Ruthenium-tungsten composite catalyst for the efficient and contamination-resistant electrochemical evolution of hydrogen, ACS Appl. Mater. Interfaces 10 (2018) 6354.
[31] I.S. Amiinu, Z. Pu, X. Liu, K.A. Owusu, H.G.R. Monestel, F.O. Boakye, H. Zhang, S. Mu, Multifunctional Mo-N/C@MoS_2 electrocatalysts for HER, OER, ORR, and Zn-air batteries, Adv. Funct. Mater. 27 (2017) 1702300.
[32] J. Yang, D. He, W. Chen, W. Zhu, H. Zhang, S. Ren, X. Wang, Q. Yang, Y. Wu, Y. Li, Bimetallic Ru-Co clusters derived from confined alloying process within zeolite-imidazolate frameworks for efficient NH_3 decomposition and synthesis, Appl. Mater. Interfaces 9 (2017) 39450.
[33] R. Ye, Y. Liu, Z. Peng, T. Wang, A.S. Jalilov, B.I. Yakobson, S.H. Wei, J.M. Tour, High performance electrocatalytic reaction of hydrogen and oxygen on ruthenium nanoclusters, ACS Appl. Mater. Interfaces 9 (2017) 3785.
[34] J. Liu, Y. Zheng, D. Zhu, A. Vasileff, T. Ling, S.Z. Qiao, Identification of pH-dependent synergy on Ru/MoS_2 interface: a comparison of alkaline and acidic hydrogen evolution, Nanoscale 9 (2017) 16616.
[35] J. Wang, K. Li, H.X. Zhong, D. Xu, Z.L. Wang, Z. Jiang, Z.J. Wu, X.B. Zhang, Synergistic effect between metal-nitrogen-carbon sheets and NiO nanoparticles for enhanced electrochemical water-oxidation performance, Angew. Chem. Int. Ed. 127 (2015) 10676.
[36] L. Zhang, W. Liu, Y. Dou, Z. Du, M. Shao, The role of transition metal and nitrogen in metal-N-C composites for hydrogen evolution reaction at universal pHs, J. Phys. Chem. C 120 (2016) 29047.
[37] H. Wang, Y. Na, L. Wei, D. Wei, C. Ke, L. Jing, L. Li, J. Wang, J. Jiang, F. Jia, Understanding the roles of nitrogen configurations for hydrogen evolution: trace atomic cobalt boost the activity of planar nitrogen doped graphene, ACS Energy Lett. 3 (2018) 1345.
[38] Z. Pu, I.S. Amiinu, Z. Kou, W. Li, S. Mu, RuP_2-based catalysts with Platinum-like activity and higher durability for hydrogen evolution reaction at all pH values, Angew. Chem. Int. Ed. 56 (2017) 11559.

Shuai Yuan received her B.S. degree from the School of Materials Science and Engineering at University of Jinan in 2016. Now she is a master student in fuel cell at Wuhan University of Technology. Her research interests focus on metal-organic frameworks (MOFs) and their applications in electrochemical energy storage.

Zonghua Pu He obtained his master degree (2015) at China West Normal University, under the supervision of Prof. Xuping Sun. He received his PhD from Wuhan University of Technology under the supervision of Prof. Shichun Mu in 2018. His research interest includes transition metal compounds preparation and application in water splitting, fuel cells and metal-air battery. Currently, he is a postdoctoral fellow at South China University of Technology.

Huang Zhou obtained his M.S. in Materials Science and Engineering under the supervision of Prof. Shichun Mu in 2017 from Wuhan University of Technology. He is now pursing his PhD degree under supervision of Prof. Yuen Wu and Yadong Li at iChEM (Collaborative Innovation Centre of Chemistry for Energy Materials), University of Science and Technology of China. His research interests focus on the design and construction of nano or sub-nano catalysts in energy conversion and storage.

Jun Yu is currently working as an associate professor at Wuhan University of Technology. He received his B.E.degree from Zhongnan University in 1994 and Ph.D.degree from Wuhan University of Technology in 2007. Afterwards, he joined the Wuhan University of Technology as researcher in 2007. He was an academic visitor at University of Waterloo (2009–2010). His research focuses on PEM fuel cell catalysts, PEM water electrolyzer and related devices. He has published dozens of papers.

Ibrahim S. Amiinu received his B.Sc. in 2008 from the Kwame Nkrumah University of Science and Technology, Ghana, and MSc/PhD degree in New Energy Materials and Devices from Wuhan University of Technology, China, in 2014/2017, respectively. His research focuses on novel synthetic mechanisms of new energy nanomaterials for application in electrochemical water splitting (HER/OER) and energy storage batteries (Zn-air and Li-ion batteries).

Jiawei Zhu obtained his B.S. in Materials Science and Engineering in 2017 from Wuhan University of Technology. He is currently a M.S. candidate in school of Material Science and Engineering from Wuhan University of Technology. His research interests focus on the design and construction of porous carbon-based materials and their application in electrochemical reactions.

Qirui Liang received his B.S. degree in 2016 from China University of Mining and Technology in Material Science and Engineering. Currently he is a research master of State Key Laboratory of Advanced Technology for Materials Synthesis and Processing, Wuhan University of Technology. His graduate tutor is Shichun Mu and now his research topic is the application of metal-organic frameworks materials in fuel cell catalysts.

Jinlong Yang received his Ph.D. degree in 2014 from Wuhan University of Technology. He was a postdoctoral fellow from 2014 to 2018 at School of Advanced Materials, Peking University, Shenzhen Graduate School, China. In 2018, he joined Stanford University, USA as a postdoctoral visiting scholar, His research interests include: energy materials (battery and catalysis), nanotechnology and electrochemistry.

Daping He is a full professor at Wuhan University of Technology. He obtained his PhD degree in Materials Processing Engineering from Wuhan University of Technology in 2013. He was a Postdoctoral Fellow in the University of Science and Technology of China. Then he joined University of Bath as a Newton International Fellow and University of Cambridge as a Postdoctoral Fellow. His research interest is preparation and application of nano composite materials into new energy devices, sensors and RF microwaves field. He has published over 70 peer-reviewed papers and 5 Chinese patents.

Zhi-Yi Hu is an associate professor within the NRC (Nanostructure Research Centre) at Wuhan University of Technology. He received his PhD degree in Physics from the University of Antwerp in 2016. His research focuses on nanostructured materials and interface characterization using advanced electron microscopy, including HR-(S)TEM, STEM-EELS and 3D electron tomography.

Gustaaf (Staf) Van Tendeloo is an emeritus professor within the EMAT (Electron Microscopy for Materials Science) research group at University of Antwerp and the director of NRC (Nanostructure Research Centre) at Wuhan University of Technology. His research focusses on the application of advanced electron microscopy (in 2D and in 3D) to materials science problems. Particular interest is on nanomaterials or nanostructured materials, porous materials and carbon based materials.

Shichun Mu is currently working as a professor at Wuhan University of Technology. He received his B.S. degree from Jilin University in 1995 and Ph.D. degree from Chinese Academy of Sciences, China in 2001. Afterwards, he joined the Wuhan University of Technology as a postdoctoral researcher, 2001–2003. He has been a full professor since 2006 at Wuhan University of Technology. He was an academic visitor at Inorganic Chemistry Laboratory, University of Oxford (2007– 2008). His research focuses on nanocarbon materials, PEM fuel cell catalysts, lithium ion battery materials and related devices. He has published over 200 papers and patents.